Variations in the Characteristic Amplitude of Tectonic Tremor Induced by Long-Term Slow Slip Events

著者	Nakamoto Keita, Hiramatsu Yoshihiro, Matsuzawa Takanori, Mizukami Tomoyuki
著者別表示	平松 良浩, 松澤 孝紀, 水上 知行
journal or publication title	Journal of Geophysical Research. Solid Earth
volume	126
number	5
page range	e2020JB021138
year	2021-04-10
URL	http://doi.org/10.24517/00062386

doi: 10.1029/2020JB021138

Variations in the characteristic amplitude of tectonic tremor induced by long-term slow slip events

Keita Nakamoto[1], Yoshihiro Hiramatsu[2], Takanori Matsuzawa[3], and Tomoyuki Mizukami[2]

[1]Graduate School of Natural Science and Technology, Kanazawa University, Kakuma, Kanazawa, 920-1192, Japan

[2]School of Geosciences and Civil Engineering, College of Science and Engineering, Kanazawa University, Kakuma, Kanazawa, 920-1192, Japan

[3]National Research Institute for Earth Science and Disaster Resilience, 3-1 Tennodai, Tsukuba, 305-0006, Japan

Correspondence author: Yoshihiro Hiramatsu

Key points:

- Long-term slow slip events change characteristic amplitudes of tectonic tremor in the episodic tremor and slip zone
- Variations in characteristic amplitude reflect the heterogeneous effective strengths of tremor patches
- Fluid migration during long-term slow slip events might control the stress state and strength of tremor patches

Abstract

Long-term slow slip events (L-SSEs) often excite short-term slow slips events (S-SSEs) and tectonic tremor in the zone of episodic tremor and slip (ETS). However, the factors controlling the occurrence of primary versus excited tremor events remain unclear. To elucidate these factors, we analyzed tectonic tremor events in and around the Bungo Channel (Nankai subduction zone), where L-SSEs are known to excite tremor and S-SSEs in the ETS zone. We focused on the spatial distribution of the characteristic amplitude (CA) of tremor, determined from the duration-amplitude distributions of tremor events, as an indicator of the properties of the tremor source. CAs are large in L-SSE slip areas and small in adjacent areas. The difference between CA values during tremor-excitation periods (L-SSEs) and the intervening periods (ΔCA) is positive in the slip area, negative in adjacent areas, and tends toward zero in the far field. We suggest that the heterogeneous distributions of CA and ΔCA reflect the heterogeneous effective strengths of tremor patches, which might be related to petrological properties, and stress and pore-fluid pressure variations induced by L-SSEs, respectively. The upward migration of fluid from the ETS zone along the plate interface might modulate the effective stress and strength states of tremor patches during L-SSEs.

Plain Language Summary

In subduction zones, slow earthquakes have inspired great interest in the connection between slow and megathrust earthquakes. Long-term slow slip events (L-SSEs) are known to excite short-term slow slip events and tectonic tremor. To understand the factors controlling the occurrence of primary and excited tremors, we investigated the characteristic amplitude (CA) of tremor events (representing the properties of a tremor source) during tremor-excitation periods and the intervening periods. CAs are larger in L-SSE slip areas than in adjacent areas during both periods. This contrast may result from differences in pore-fluid pressure arising from differences in petrological properties between the two areas. Moreover, relative to CAs during the intervening periods, CAs during tremor-excitation periods are larger in the slip area, smaller in adjacent areas, and almost the same far from the slip area. These variations in CA are the combined effects of (1) stress changes accompanying L-SSEs and (2) upward fluid migration along the plate interface from the tremor source area during L-SSEs, because fluid migration reduces the pore-fluid pressure and increases the strength of tremor source areas. Our findings emphasize that CA can be a useful tool for monitoring fluid migration in the source areas of tremor events.

1. Introduction

Recent discoveries of slow earthquakes have revealed the diversity of slip phenomena and subduction dynamics worldwide. Slow earthquakes are usually classified into long-term slow slip events (L-SSEs, durations of months to years; e.g., Ozawa et al., 2002), short-term slow slip events (S-SSEs, durations of days to weeks; e.g., Dragert et al., 2001), very-low-frequency (VLF) earthquakes (e.g., Ito et al., 2007), low-frequency earthquakes (LFEs; e.g., Katsumata & Kamiya, 2003), and tectonic tremor (e.g., Obara, 2002). Slow earthquakes show characteristic scaling relationships that separate them from regular earthquakes. For example, Ide et al. (2007) proposed that the seismic moment of a slow earthquake is proportional to its duration, although the seismic moments of SSEs in Cascadia (Michel et al., 2019) and LFEs in Shikoku, Japan (Supino et al., 2020), are reported to be proportional to the cube of their duration, as observed for regular earthquakes. The duration-amplitude distribution of tremor events obeys an exponential distribution rather than a power-law distribution as usually observed for regular earthquakes (Watanabe et al., 2007). This indicates the existence of a characteristic or mean tremor amplitude that is proportional to the geometric dimensions of the tremor source (Benoit et al., 2003). Exponential distributions have also been reported for the size-frequency (Hiramatsu et al., 2008) and size-energy rate distributions of tremor events (Yabe & Ide, 2014). However, power-law distributions with and without an exponential taper were observed in the size-frequency distributions of shallow tremors in the Nankai Trough (Nakano et al., 2019) and LFEs in Cascadia (Bostock et al., 2015), respectively. These features are well explained by statistical models of slow earthquakes; for example, a Brownian model reproduces well the exponential scaling of duration-amplitude distributions (Ide, 2008) and the power-law scaling with an exponential taper of cumulative size distributions (Ide & Yabe, 2019).

The spatial distribution of slow earthquakes is highly variable among subduction zones and, therefore, is regarded as a unique feature providing insight into the relationship between slow and megathrust earthquakes (e.g., Nishikawa et al., 2019; Obara & Kato, 2016). Interactions between slow earthquakes are also an important process in subduction dynamics. Spatiotemporally coincident S-SSEs and tremor are termed episodic tremor and slip (ETS) events (e.g., Rogers & Dragert, 2003). L-SSEs are distributed around the source areas of megathrust earthquakes in the Nankai (Suito & Ozawa, 2009), Hikurangi (Wallace & Beavan, 2010), and Mexican subduction zones (Correa-Mora et al., 2008; Radiguet et al., 2012), and L-SSEs have been observed to trigger ETS events (e.g., Hirose & Obara, 2005).

The Bungo Channel (western Shikoku, Japan; Figure 1), in the Nankai subduction zone, is one of the most active regions of slow earthquakes. There, L-SSEs are known to modulate ETS events (Hirose

& Obara, 2005; Ozawa et al., 2013). Tremor beneath the Bungo Channel is characterized by higher radiation of seismic energy relative to that in the surrounding area (Kano et al., 2018; Yabe & Ide, 2014). Kano et al. (2018) attributed this to heterogeneity of effective strength in tremor source patches, which is controlled by pore-fluid pressure. Obara (2010) found that tremor on the up-dip side of the ETS zone is triggered by L-SSEs, and that increased tremor activity there is coincident with L-SSE occurrence. Interestingly, the up-dip side is included in the slip area of L-SSEs (Nakata et al., 2017). In contrast, tremor is steadily active on the down-dip side of the ETS zone, irrespective of L-SSE occurrence. This complicated relationship between L-SSEs and ETS events beneath the Bungo Channel raises the question of whether there are any differences in the physical conditions of tremor sources during L-SSEs and intervening periods. If such differences exist, the characteristics of tremor signals might be expected to change accordingly.

In this study, to understand the variable occurrence of tremor in western Shikoku, Japan, we separately analyzed tremor events during L-SSEs and intervening periods in the Bungo Channel. We used the characteristic amplitude (CA), which is estimated from the duration-amplitude distribution of a tremor event, as an indicator of the properties of the tremor source. We detected a significant difference in the CA of tremors between the two periods. Based on spatial and temporal variations in CA, and previous tremor observations, we document that the strengths of tremor patches are modulated by stress disturbances and fluid migration associated with L-SSEs.

2. Data

Our study area was in the Bungo Channel (Figure 1a), where past L-SSEs are known to have activated tremor and S-SSEs (Hirose & Obara, 2005; Ozawa et al., 2013). We analyzed the vertical component of velocity waveform data recorded at five National Research Institute for Earth Science and Disaster Resilience (NIED) Hi-net stations in western Shikoku (HIYH, KWBH, OOZH, TBEH, and IKKH; Figure 1b), which have also been used in previous studies (Daiku et al., 2018; Hirose et al., 2010b). Hirose et al. (2010b) reported that these stations provide high S/N (signal-to-noise ratio) waveform data for tremors. In general, the horizontal components are useful for analyzing *S* waves. However, the S/N of the vertical component is usually higher than that of the horizontal ones, and Ueno et al. (2010) used vertical-component waveform data from arrays in western Shikoku for this reason. We used tremor catalogues provided by NIED: the hybrid catalogue (Maeda & Obara, 2009) was used to search for tremor events and to visually check waveforms (see subsection 3.1). Therefore, the tremors analyzed in this study correspond to at least one hypocenter in the hybrid catalog. The location of a tremor event was assigned to a hypocenter in the hybrid clustering catalog (Obara et al., 2010) corresponding to the time of the tremor.

Data on tremors occurring after February 2016 were not included in our analysis because tremors activated by the 2016 L-SSE have not yet been confirmed, and because the timing of the end of that L-SSE is unclear (Ozawa, 2017). Therefore, we analyzed the period from January 2001 to January 2016 (Figure 1b), excluding two periods during which L-SSEs in nearby central-western Shikoku were active (Takagi et al., 2016). Takagi et al. (2016) suggested that these L-SSEs triggered tremor, even in western Shikoku, although the triggered tremors were minor and are hard to recognize in Figure 1b. These L-SSEs were M_w 6.0–6.3, comparable to short-term SSEs in this region. In contrast, the magnitudes of L-SSEs in the Bungo Channel, especially the M_w 7.1 and 6.9 events in 2003 and 2010, respectively (Nakata et al., 2017), are much larger than those of L-SSEs in central-western Shikoku, implying that the L-SSEs in central-western Shikoku have less impact on tremor activity. Furthermore, the fault models for these L-SSEs were estimated by using rectangular faults with uniform slip (Takagi et al., 2016), making it difficult to evaluate the spatial relationship between the slip areas of the L-SSEs and tremor characteristics, as was conducted for L-SSEs in the Bungo channel. Thus, it is not appropriate to treat L-SSEs in central-western Shikoku in the same way as those in the Bungo Channel.

3. Method

3.1 Reduced Displacement, Apparent Moment, and Apparent Moment Rate

We used reduced displacement (Aki & Koyanagi, 1981) as tremor amplitude in our analysis. The reduced displacement of a body wave, corrected for geometrical spreading, is calculated as $D_R = A \cdot r$ (Aki & Koyanagi, 1981), where A is the root-mean-squared peak-to-peak amplitude (m) and r is the source-station distance (m).To calculate A, we applied a band-pass filter between 2 and 10 Hz to the vertical component of the velocity waveform and a moving average with a time window of 6 s (Watanabe et al., 2007).

To identify tremor events, we defined the noise level in D_R hourly at each station, and manually excluded regular earthquakes and other impulsive noises by visual inspection. We calculated the noise level from 5-minute signal-free records in which no earthquakes, tremors, or artificial signals were included (Hirose et al., 2010b). Tremor events were then identified as events (1) starting and ending when D_R exceeded and fell below the noise level, respectively, (2) with durations longer than 1 minute, and (3) with maximum D_R at least two times the noise level (Figure 2a). We used apparent moment, the time integral of D_R over the tremor duration, as an indicator of tremor magnitude (Hiramatsu et al., 2008). The apparent moment rate was estimated as the apparent moment divided by tremor duration.

3.2 Characteristic Amplitude of Tremor

Here we introduce characteristic amplitude, CA, a new parameter sensitive to the size and growth of a tremor source. We investigated the scaling relationship between tremor duration and amplitude by varying the amplitude threshold (Figure 2a) and measuring the sum of the durations when tremor amplitude exceeded that threshold (Watanabe et al., 2007). We then compared exponential and power-law scaling models of the duration-amplitude distribution. The exponential model is expressed as:

$$\mathrm{d}(D_R^*) = d_t e^{-\lambda D_R^*}, \qquad (1)$$

where $\mathrm{d}(D_R^*)$ is the total duration (s) for which the tremor amplitude exceeds the threshold value (D_R^*), λ is the slope of the best-fit line estimated by the least-squares method (Figure 2b), and d_t is the prefactor (s). Thus, d_t is interpreted as the noise-free (zero-amplitude) duration.

The power-law model is expressed as:

$$\mathrm{d}(D_R^*) = d_t (D_R^*)^{-\gamma}, \qquad (2)$$

where γ is the slope of the best-fit line (Figure 2c). The goodness of fit, represented by the distribution of the coefficients of determination (R^2), of each model shows that the exponential model better fits observed tremor duration-amplitude distributions than the power-law model (Figure 3). A similar result has been reported for tremor characteristics in the Tokai region, central Japan (Watanabe et al., 2007), implying that exponential tremor duration-amplitude distributions are common to much of the Nankai subduction zone.

For each tremor event, we calculated λ by fitting the exponential model to the duration-amplitude distribution at each station, averaged λ over the stations with $R^2 \geq 0.8$, and adopted the inverse of the average λ as the CA for that event. The inverse of λ at each station was typically within a factor of 2 of the CA for an event.

3.3 Determination of Tremor-excitation Periods

We hereafter refer to periods in which an L-SSE was geodetically detected in the Bungo Channel as 'L-SSE periods' (Ozawa, 2017; Ozawa et al., 2013) and periods in which no L-SSE was detected around western Shikoku (Ozawa, 2017; Ozawa et al., 2013; Takagi et al., 2016) as 'inter-L-SSE periods'. It is known that tremor events in western Shikoku are activated during L-SSE periods (Ozawa et al., 2013). The slope of the cumulative apparent moment trend is distinctly steeper during

L-SSE periods than during inter-L-SSE periods (Figure 4a), indicating the excitation of tremor events by L-SSEs (Annoura et al., 2016; Daiku et al., 2018; Kono et al., 2020). However, observed tremor activity varies greatly, even among L-SSE periods. Therefore, to focus only on tremors causally induced by an L-SSE, we define 'tremor-excitation periods' as follows.

To quantitatively evaluate tremor-excitation periods, we defined a 0.05° × 0.05° grid and collected tremor events observed within 10 km of each grid point. We calculated a tentative tremor excitation ratio as the ratio of the apparent moment rate during one month to that during inter-L-SSE periods. The apparent moment rate during inter-L-SSE periods was calculated as the total apparent moment during those periods divided by their total duration.

To emphasize the change of the cumulative apparent moment, we used only events at grid points with tentative excitation ratios >4.0. The distribution of tremor events with high excitation ratios was restricted to the up-dip side of the ETS zone in the western part of the study area (Figure 1b), consistent with previous studies (e.g., Hirose et al., 2010a; Obara et al., 2010). We then smoothed the cumulative apparent moment trend using a moving average with a window of 101 events, i.e., 50 events before and after a target event (Figure 4b), to reduce spike-like variations in apparent moment release rate.

Finally, using the smoothed cumulative apparent moment trend, we determined tremor-excitation periods as periods (1) coincident with one of the geodetically determined L-SSE periods, (2) with apparent moment rates more than twice the average during inter-L-SSE periods, and (3) with maximum apparent moment rates at least five times the average during inter-L-SSE periods (Figure 4c). The determined tremor-excitation periods are shown as red bars in Figures 1b and 4c. The period of the L-SSEs in central-western Shikoku (gray zones in Figures 4a and 4b) was characterized by a low apparent moment rate. We then analyzed tremor events during tremor-excitation periods separately from those during inter-L-SSE periods to reveal differences in the CAs of tremors between those periods.

4. Results and Discussion

4.1 Relationship between CA, Apparent Moment, and Apparent Moment Rate

To clarify the meaning of CA, we here investigated the relationships between CA, apparent moment, and apparent moment rate of tremor events (Figure 5). The estimated CA and apparent moment, together with the start time, duration, and location of tremor events, are summarized in

Table S1 in the supporting information. For the 8,484 tremors analyzed herein, we obtained statistically significant positive correlations ($p < 10^{-15}$) between CA and the other parameters. This means that events with larger CAs had relatively large apparent moments and apparent moment rates. Because a large apparent moment rate corresponds to a large seismic-energy radiation rate, these results show that CA is a fundamental parameter closely related to the size and seismic-energy radiation rate of a tremor event. Integrating equation (1) from 0 to infinity for D_R^* provides the analytical relationship among the apparent moment, CA, and d_t: apparent moment = CA$\cdot$ d_t. This formula indicates that CA is the average apparent moment rate and that the size of tremor scales as d_t. Given that d_t is the noise-free duration and is generally larger than the observed duration of a tremor event, the observed duration roughly satisfies this relationship (Figure 5a). Furthermore, the apparent moment rate appears to be independent of the observed tremor duration (Figure 5b).

4.2 Spatial Distribution of CA

Figure 6 shows examples of size-frequency distributions for CA, during both the tremor-excitation and inter-L-SSE periods, on the same grid (Figures 7a and 7b). The exponential distribution shows a better fit than the power-law distribution, as was shown for seismic energy radiation rate (Yabe & Ide, 2014). Figure 7 compares the spatial distribution of median CA values during tremor-excitation and inter-L-SSE periods to the slip distribution of the 2010 L-SSE (Nakata et al., 2017). The median CA values calculated for tremor events within 10 km of each grid point can be regarded as typical of the area around each grid point; a similar treatment was adopted for tremor seismic-energy radiation rate by Yabe and Ide (2014). Only grid points including more than 100 events in both periods are included in the maps.

The obtained CA values were mostly restricted at the up-dip side of the ETS zone (Figure 7). Median CA values were relatively high within the slip area of the 2010 L-SSE and relatively low outside that area. The area characterized by high median CA values overlapped the area in which tremor events were strongly excited during L-SSEs (Figure 1b). The spatial distribution of CAs during tremor-excitation periods was similar to that during inter-L-SSE periods, suggesting that the observed tremor characteristics reflect inherent structures on the plate interface.

Obara et al. (2010) reported a bimodal depth distribution for tremor events in and around the Bungo Channel. Interestingly, tremor activity of nearly constant magnitude occurs regularly on the down-dip side of the ETS zone, whereas increased tremor activity occurs on the up-dip side during L-SSEs. Obara et al. (2010) suggested that the plate-coupling strength on the up-dip side is stronger than that down dip. Yabe and Ide (2014) reported high seismic-energy radiation rates for tremor events on the up-dip side (confirmed by Kano et al., 2018) and suggested the existence of tremor patches with high strength there. Therefore, considering the positive correlation between CA and apparent moment, and apparent moment rate (Figure 5), we interpret that high (low) CA values indicate the existence of large (small) and/or strong (weak) tremor patches.

The high-CA tremors identified herein occurred within the down-dip portion of the L-SSE area beneath the Bungo Channel. Numerical studies have shown that bimodal slow-slip behaviors similar to that observed in the Nankai subduction zone can be reproduced by slightly less-elevated pore pressures in L-SSE areas relative to ETS zones (Matsuzawa et al., 2010). Our results thus highlight an intermediate state of plate coupling between the weak, chattering ETS zone and the strong, silent L-SSE area that is possibly controlled by the fluctuation in pore pressures.

Ando et al. (2012) proposed a theoretical model for tremor generation, termed the 'patch model', according to which tremor results from sequential ruptures of brittle tremor patches distributed within a ductile fault area. In western Shikoku, Kano et al. (2018) found that the energy radiated by tremor events is positively correlated with tremor migration speed and SSE slip rate, and they updated the patch model of Ando et al. (2012) to account for the V_P/V_S distribution of the overriding plate (Nakajima & Hasegawa, 2016). Tremor patches of different strengths are heterogeneously distributed depending on pore-fluid pressure variations. This model explains the observations of heterogeneous tremor properties in Shikoku; that is, tremor patches with high effective strength and caused by low fluid pressure occur in the western part, whereas ones with low effective strength caused by high fluid pressure occur in the central part. The CA distribution observed herein is consistent with this model, although we must consider this new constraint that strong tremor patches are dominant in the L-SSE area beneath the Bungo Channel.

The spatial variation in the strength of tremor sources might also be explained from a petrological viewpoint. Mizukami et al. (2014) proposed that fluid pressure on the plate interface may vary depending on the mineral assemblages in the hanging wall mantle beneath western Shikoku. The dominant mineral assemblage in the hydrated mantle wedge changes from Atg (antigorite) + Brc (brucite) to Atg + Ol (olivine) with increasing temperature. The petro-structural nature of these serpentinites implies that Atg + Brc assemblages are more permeable, and thus can absorb more water, than Atg + Ol assemblages. The metamorphic transition is variable depending on the bulk chemistry of the mantle (Mg/Fe ratio, Al_2O_3 content, etc.), among other factors (Mizukami et al., 2014). A mixed lithology comprising both Atg + Brc and Atg + Ol serpentinites in the mantle wedge may explain the intermediate state of plate coupling revealed by our CA analysis.

Ji et al. (2016) made a model calculation for the thermal structure of the Nankai subduction zone in which the effects of corner flow in the mantle wedge are considered more significant than indicated in previous works, and, as a result, temperatures on the plate interface are higher. If such hot geothermal conditions are developed beneath western Shikoku, spatial variations in the serpentinite mineral assemblage cannot be assumed for this region, and another petrological explanation for the heterogeneous pore-fluid pressure distribution is required.

Tectonically, the coincident distribution of high-CA areas in the L-SSE area may suggest a possible contribution of the occurrence of L-SSEs to the development of the strong tremor patches there. Semi-continuous and repeated displacements during L-SSEs likely cause fractures along the slip plane that may connect fluid pathways between the down-dip ETS zone of higher pore pressure and the up-dip L-SSE area of lower pore pressure. The intermediate pore pressures expected for high-energy and high-CA tremors could thus be attained under a fluid flux along the plate boundary between these contrasting areas.

4.3 Effects of L-SSEs on CA Variations

To examine the effects of L-SSEs on tremor strength, we compared the CA values during tremor-excitation periods with those during inter-L-SSE periods at each grid point. In general, if relatively high-strength patches (i.e., large patches and/or those with sustained stresses) are activated during L-SSEs, the difference between the CAs during the two periods ($\Delta CA_1 = CA_{tremor\text{-}excitation} - CA_{inter\text{-}L\text{-}SSE}$) is positive, whereas ΔCA_1 is negative if weaker patches are activated by L-SSEs. We applied the nonparametric bootstrap method to evaluate the relative error on the median CA value. The bootstrap sample size is the same as that used at each grid point. From 2,000 bootstrap estimations, we obtained averages and standard deviations on the relative errors of the median CA values of 0.056 and 0.014, respectively, for tremor excitation periods and 0.055 and 0.016, respectively, for inter L-SSE periods. Therefore, a typical error on ΔCA_1 is approximately 1×10^{-6} m^2.

Figure 7c shows a distinct spatial variation of ΔCA_1 in terms of distance from the 2010 L-SSE in the Bungo Channel (see Figure 1b for temporal variations of CA). Based on the along-strike variations in ΔCA_1, we divided the study area into three zones from west to east: zone A with positive ΔCA_1, zone B with negative ΔCA_1, and zone C with ΔCA_1 values around zero (Figure 7c). ΔCA_1 values are positive within the slip area of the L-SSE, negative in the eastern periphery of the slip area, and tend toward zero in the far field. Values of zero indicate that the stress conditions and dynamic properties of tremor sources are not affected by L-SSE occurrence, as for the regular tremor activity in zone C (Figure 1b). Furthermore, we adopted the Brunner-Munzel test (Brunner

& Munzel, 2000; Neubert & Brunner, 2007), a nonparametric test of stochastic equality between two samples, to evaluate the statistical significance of ΔCA_1 values at each grid point (Figure 7d). Orange to red grid points in Figure 7d, which correspond mainly to positive ΔCA_1 values in zone A and negative ΔCA_1 values in zone B, indicate that the ΔCA_1 values at those grid points are statistically significant at a significance level of 0.05.

To examine whether the variations in median CA values shown in Figure 7 may be typical of L-SSEs, we investigated the variations in median CA values of each L-SSE in the Bungo Channel (Figure 8). Here, we defined ΔCA_2 as the difference in median CA value between each L-SSE period (limited to tremor-excitation) and the inter L-SSE periods ($\Delta CA_2 = CA_{\text{L-SSE + tremor–excitation}} - CA_{\text{inter-L-SSE}}$). In Figure 8, we used grid points including more than 50 events in the tremor-excitation periods of each L-SSE because of the small number of events during those periods; therefore, the ΔCA_2 trends in Figure 8 tend to emphasize temporally localized variations in median CA. The median CA and ΔCA_2 values in zones A and B are consistent with those in Figure 7, although the observations are insufficient for the 2014 L-SSE, the smallest (M_w ~6.2) of the three L-SSEs (Ozawa, 2017). The differences in CA and ΔCA_2 values in zone C among the L-SSEs suggest that these variations might not have a common origin nor be related to the occurrence of L-SSEs because the tremor activity in zone C appears to be little modulated by the L-SSEs (Figure 1b).

To test whether stress disturbances due to L-SSEs are a dominant cause of the observed variations in median CA values in zone B (Figure 7), we focused on median CA and the difference in CA values in the initial stages of the 2003 and 2010 L-SSEs (Figure 9), that is, the median CA values during the L-SSE period before tremor-excitation (the portions of blue bars preceding red bars in Figures 1b and 4c) compared to the median CA value during the L-SSE period with tremor-excitation ($\Delta CA_3 = CA_{\text{L-SSE – tremor–excitation}} - CA_{\text{L-SSE + tremor–excitation}}$) (top and middle panels, Figure 9). We used grid points including more than 50 events in each L-SSE period excluding/including tremor-excitation. For the 2003 event, we obtained median CA and positive ΔCA_3 values mainly at grid points in zone C (top-left, Figure 9), which might be a temporally localized variation. Indeed, stacking the 2003 and 2010 L-SSE data shows ΔCA_3 values around zero at most grid points in zone C (bottom-right, Figure 9). For the 2010 event, the median CA values are relatively small in all zones, and negative ΔCA_3 values are observed in zone A (middle panels, Figure 9). In the stacked 2003 + 2010 data, ΔCA_3 values are strongly negative in zone A and weakly negative in zone B (bottom panels, Figure 9). The strongly negative ΔCA_3 values in zone A suggest that stress disturbances during the initial stages of L-SSEs might increase the rupture of tremor patches with weak effective strengths. In contrast, the weakly negative ΔCA_3 values in zone B might indicate that the initial stress disturbances do not greatly alter the CA values of ruptured tremor patches compared to those during the tremor-excitation periods.

Figure 10 shows changes of the frequency distributions of CA in zones A and B, depicting the proportions of tremors causally responsible for positive and negative ΔCA_1 values. To reduce the effect of CA fluctuations, all panels of Figure 10 include only grid points with ΔCA_1 values $\geq 1.0 \times 10^{-6}$ m^2 or $\leq -1.0 \times 10^{-6}$ m^2. Positive ΔCA_1 values in zone A result from the increased occurrence of high-CA tremor and the decreased occurrence of low-CA tremor during tremor-excitation periods (bottom panel, Figure 10b). The increased occurrence of high-CA tremor suggests that the effective strength of tremor patches during tremor-excitation periods is larger than that during inter-L-SSE periods. This result can be interpreted as an increased probability of rupturing stronger and/or larger patches under the increased shear stresses associated with L-SSEs. The relatively decreased occurrence of low-CA tremor may represent that tremor patches easily grow to larger sizes under conditions of greater stress.

Annoura et al. (2016) attributed increased tremor activity around the Bungo Channel to stress disturbances induced by L-SSEs. Here, we consider that zone B (negative ΔCA_1, Figure 7c) corresponds to the area of relatively large stress change during the SSE, whereas zone C is sufficiently distant from the slip area that no significant stress change occurred. In zone B, we recognize the increased occurrence of tremor with intermediate CA and the decreased occurrence of high-CA tremor (bottom panel, Figure 10c). As mentioned above, a small CA value reflects a relatively weak effective strength of a given tremor patch. Therefore, these results imply that stress disturbances effectively enhance the rupture of tremor patches with weak to moderate effective strengths in zone B. Moreover, the decreased occurrence of high-CA tremor in zone B suggests that tremor sources were unable to grow markedly during the tremor-excitation period. Such suppressed tremor-source growth might be possible if the increases in strength of high-CA tremor patches outweighed the increases in stress induced by L-SSEs.

If these geodynamic interpretations of positive and negative ΔCA_1 values are correct, fluid migration might be responsible for the increased effective strength of tremor patches during tremor-excitation periods (Figure 11). Recently, Tanaka et al. (2018) observed temporal gravitational changes related to L-SSEs in Tokai, which they reproduced by numerically modeling poroelastic fluid flow up-dip from the ETS zone along the plate interface. Kano et al. (2019) also stressed the importance of upward fluid migration from the ETS zone, through the L-SSE zone, and to the down-dip edge of the locked seismogenic zone to explain simultaneous transient slip in the two major slip patches, i.e., the ETS zone and the down-dip edge of the locked seismogenic zone. If such upward fluid migration through the slip plane occurs during L-SSEs in western Shikoku, reduced pore-fluid pressure in the ETS zone could result in the increased effective strength of tremor patches. Therefore, we conclude that the stress increase during L-SSEs, which is large enough to rupture tremor patches with high effective strength, generates high-CA tremors (Figure 11).

4.4 Implications of CA for slow earthquakes

The envelope of the reduced displacement may be interpreted as an apparent moment rate function (Hiramatsu et al., 2008). Therefore, by applying appropriate corrections, we can convert CA to a characteristic moment rate, although it is a band-limited estimation. Assuming that each tremor pulse consists of an *S* wave, we multiplied CA by $4\pi\rho\beta^3$, and corrected for the effects of intrinsic attenuation and the average radiation pattern using the intrinsic attenuation factor Q = 184, center frequency f = 6 Hz, *S*-wave velocity β = 3,500 m/s, density ρ = 2,700 kg/m^3 (Maeda & Obara, 2009), the average *S*-wave radiation pattern of 0.63. This rough estimation provides the term for the conversion from CA to characteristic moment rate as 10^{16} N/m/s, resulting in characteristic moment rates of 10^{10}–10^{12} Nm/s.

Interestingly, this estimated characteristic moment rate is similar to seismic moment rates previously reported for slow earthquakes. Kao et al. (2010) reported the seismic moments of tremor bursts with durations 1–5 s in Cascadia to be 10^{10}–10^{12} Nm, resulting in seismic moment rates on the same order as the characteristic moment rate obtained herein. Sweet et al. (2019) found that the seismic moment size-frequency distributions of four LFE families in Cascadia follow an exponential rather than a power-law distribution. They estimated a characteristic seismic moment on the order of 10^{11} Nm. This provides a characteristic LFE moment rate consistent with that estimated in this study, 10^{10} Nm/s, if the typical duration of those LFEs is 10 s. The linear relationship between the areas of tremor episodes and the seismic moments of SSEs in the Nankai subduction zone (Obara et al., 2010) might similarly reflect the characteristic moment rate of tremor.

Some VLF events provide seismic moment rates of 10^{13} Nm/s (Ide et al., 2008; Matsuzawa et al., 2009), an order of magnitude higher than the characteristic moment rate of tremor estimated herein, whereas others show similar seismic moment rates of 10^{11}–10^{12} Nm/s (Ide & Yabe, 2014; Ide, 2016; Maury et al., 2016). SSEs in the Nankai, Cascadia, and Mexico subduction zones show seismic moment rates of 10^{12}–10^{13} Nm/s (Sekine et al., 2010; Schmidt & Gao, 2010; Graham et al., 2016; Rousset et al., 2017), close to or above the upper bound of our estimate, and Hawthorne et al.

(2016) reported seismic moment rates on the order of 10^{12} Nm/s for SSEs during rapid tremor reversals. We suggest that the order-of-magnitude similarity between the seismic moment rates of slow earthquakes and the characteristic moment rate is a fundamental property of the broad linear relationship between seismic moment and duration for slow earthquakes (Ide et al., 2007).

The characteristics of slow earthquakes can be reproduced by conceptual models such as the Brownian model (Ide, 2008; Ide & Maury, 2018) and the patch model (Ando et al., 2010, 2012; Nakata et al., 2011). One of the key parameters of the Brownian model is the characteristic time, the reciprocal of which is the dampening coefficient for a temporally varying source radius; a larger characteristic time thus provides a larger moment rate. However, as shown by Ide and Maury (2018), the dependence of seismic moment rate on the characteristic time is systematically less obvious for seismic moments $\leq 10^{14}$ Nm. Therefore, variations in the characteristic time might not be plausible as the cause of the observed variations in CA values induced by L-SSEs.

The patch model consists of clusters of frictionally unstable patches on a stable background, where each cluster of patches corresponds to a tremor source. The variation in the patch distribution and/or the viscosity of the patch/background controls the moment rate function. A higher moment rate is reproduced by a denser patch distribution or a lower patch/background viscosity (Nakata et al., 2011). The positive ΔCA_1 values in zone A imply a relatively higher characteristic moment rate for tremors during tremor-excitation periods. If this is the case, an increase in CA may be interpreted as an increase in the size of a single patch and/or in the density of patches in the tremor source, with the increased patch size or density enhancing the effective strength of the tremor source.

5. Conclusions

We investigated tectonic tremor events in and around the Bungo Channel (Nankai subduction zone), where L-SSEs are known to induce ETS events, to reveal the difference between primary and induced tremor events. We used the characteristic amplitude (CA), estimated from the duration-amplitude distribution of a tremor event, as an indicator of the size and the strength of a tremor source patch. The spatial distribution of CA is characterized by large and small values in L-SSE slip areas and adjacent areas, respectively, suggesting that stronger tremor patches are distributed in the slip area and weaker patches outside the slip area. This distribution might reflect variations in pore-fluid pressure, which is controlled by serpentinite mineral assemblages. The difference between the CA values during tremor-excitation periods and those during inter-L-SSE periods (ΔCA_1) is positive in the L-SSE slip area, negative in adjacent areas, and tends toward zero in the far field. We suggest that this spatial distribution results from increased stress, which decreases with distance from the slip area, and increased effective strength of tremor patches during L-SSEs, which may result from upward fluid migration from the ETS zone along the plate interface. This heterogeneous distribution of effective stress/tremor-patch strength, modulated by stress changes and fluid migration induced by L-SSEs, might cause the heterogeneous ΔCA_1 distribution. In other words, the observed CA heterogeneity illustrates transient states of heterogeneous fluid pressure fluctuations caused by L-SSEs along the plate interface.

Acknowledgments. We used waveform data recorded by Hi-net and the NIED catalogue of tectonic tremor hypocenters. The figures were produced using Generic Mapping Tools (Wessel and Smith, 1998). Comments from anonymous reviewers were useful to improve the manuscript.

Data Availability Statement

The Hi-net waveform data used herein is available online through the NIED Hi-net website (https://www.hinet.bosai.go.jp/?LANG=en). The NIED hybrid clustering tremor catalogue can be downloaded from the Slow Earthquake Database (http://www-solid.eps.s.u-tokyo.ac.jp/~sloweq/) and the NIED hybrid tremor catalog is available online through the NIED repository (https://quaketm.bosai.go.jp/~tkmatsu/tremor_catalog/NIED_tremor_hybrid_W_Shikoku_Jan2001-Jan2016.txt).

References

Aki, K., & Koyanagi, R.Y. (1981). Deep volcanic tremor and magma ascent mechanism under Kilauea, Hawaii. *Journal of Geophysical Research,* **86**, 7095-7109. https://doi.org/10.1029/JB086iB08p07095

Ando, R., Nakata, R., & Hori, T. (2010). A slip pulse model with fault heterogeneity for low-frequency earthquakes and tremor along plate interfaces, *Geophysical Research Letters*, **37**, L10310. https://doi.org/10.1029/2010GL043056

Ando, R., Takeda, N., & Yamashita, T. (2012). Propagation dynamics of seismic and aseismic slip governed by fault heterogeneity and Newtonian rheology. *Journal of Geophysical Research: Solid Earth,* **117**, B11308. https://doi.org/10.1029/2012JB009532

Annoura, S., Obara, K., & Maeda, T. (2016). Total energy of deep low-frequency tremor in the Nankai subduction zone, southwest Japan. *Geophysical Research Letters,* **43**, 2562–2567. https://doi.org/10.1002/2016GL067780

Benoit, J.P., McNutt, S. R., & Barboza, V. (2003). Duration-amplitude distribution of volcanic tremor. *Journal of Geophysical Research: Solid Earth*, **108**(B3), 2146 https://doi.org/10.1029/2001JB001520

Bostock, M. G., Thomas, A. M., Savard, G., Chuang, L., & Rubin, A. M. (2015). Magnitudes and moment-duration scaling of low-frequency earthquakes beneath southern Vancouver Island, *Journal of Geophysical Research: Solid Earth*, **120**, 6329– 6350. https://doi.org/10.1002/2015JB012195

Brunner, E., & Munzel, U. (2000). The Nonparametric Behrens-Fisher Problem: Asymptotic Theory and a Small-Sample Approximation. *Biometrical Journal* **42** (1): 17–25. https://doi.org/10.1002/(SICI)1521-4036(200001)42:1<17::AID-BIMJ17>3.0.CO;2-U

Correa-Mora, F., DeMets, C., Cabral-Cano, E., Marquez-Azua, B., & Diaz-Molina, O. (2008). Interplate coupling and transient slip along the subduction interface beneath Oaxaca, Mexico. *Geophysical Journal International*, **175**, 269–290. https://doi.org/10.1111/j.1365-246X.2008.03910.x

Daiku, K., Hiramatsu, Y., Matsuzawa, T., & Mizukami, T. (2018). Slow slip rate and excitation efficiency of deep low-frequency tremors beneath southwest Japan. *Tectonophysics*, **722**, 314-323. https://doi.org/10.1016/j.tecto.2017.11.016

Dragert, H., Wang, K., & James, T. S. (2001). A Silent slip event on the deeper Cascadia subduction interface. *Science*, **292**, 1525–1528. https://doi.org/10.1126/science.10160152

Graham, S., DeMets, C., Cabral-Cano, E., Kostoglodov, V., Rousset, B., Walpersdorf, A., Cotte, N., Lasserre, C., McCaffrey, R., & Salazar-Tlaczani, L. (2016). Slow slip history for the Mexico subduction zone: 2005 through 2011. *Pure and Applied Geophysics*, **173**(10–11), 3445–3465. https://doi.org/10.1007/s00024-015-1211-x

Hawthorne, J. C., M. G. Bostock, A. A. Royer, & A. M. Thomas (2016). Variations in slow slip moment rate associated with rapid tremor reversals in Cascadia, *Geochemistry, Geophysics, Geosystems*, **17**, 4899–4919. https://doi.org/10.1002/ 2016GC006489

Hiramatsu, Y., Watanabe, T., & Obara, K. (2008). Deep low-frequency tremors as a proxy for slip monitoring at plate interface. *Geophysical Research Letters,* **35**, L13304.

https://doi.org/10.1029/2008GL034342

Hirose, H., & Obara, K. (2005). Repeating short-and long-term slow slip events with deep tremor activity around the Bungo channel region, southwest Japan. *Earth Planets Space*, **57**(10), 961–972. https://doi.org/10.1186/BF03351875

Hirose, H., Asano, Y., Obara, K., Kimura, T., Matsuzawa, T., Tanaka, S., & Maeda, T. (2010a). Slow earthquakes linked along dip in the Nankai subduction zone. *Science*, **330**, 1502. https://doi.org/ 10.1126/science.1197102

Hirose, T., Hiramatsu, Y., & Obara, K. (2010b). Characteristics of short-term slip events estimated from deep low-frequency tremors in Shikoku, Japan. *Journal of Geophysical Research: Solid Earth*, **115**, B10304. https://doi.org/10.1029/2010JB007608

Ide, S. (2008). A Brownian walk model for slow earthquakes, *Geophysical Research Letters*, **35**, L17301, doi:10.1029/ 2008GL034821

Ide, S. (2016). Characteristics of slow earthquakes in the very low frequency band: Application to the Cascadia subduction zone, *Journal of Geophysical Research: Solid Earth*, **121**, 5942– 5952. https://doi.org/10.1002/2016JB013085

Ide, S., Beroza, G., Shelly, D., & Uchide, T. (2007). A scaling law for slow earthquakes. *Nature,* **447,** 76–79. https://doi.org/10.1038/nature05780

Ide, S., Imanishi, K., Yoshida, Y., Beroza, G. C. & Shelly, D. R. (2008). Bridging the gap between seismically and geodetically detected slow earthquakes, *Geophysical Research Letters*, **35**, L10305, doi:10.1029/2008GL034014

Ide, S., & Maury, J. (2018). Seismic moment, seismic energy, and source duration of slow earthquakes: Application of Brownian slow earth- quake model to three major subduction zones. *Geophysical Research Letters*, *45*, 3059–3067. https://doi.org/10.1002/ 2018GL077461

Ide, S., & Yabe, S. (2014). Universality of slow earthquakes in the very low frequency band. *Geophysical Research Letters*, **41**(8), 2786–2793. https://doi.org/10.1002/2014GL059712

Ide, S., & Yabe, S. (2019). Two-Dimensional Probabilistic Cell Automaton Model for Broadband Slow Earthquakes. *Pure and Applied Geophysics,* **176,** 1021–1036. https://doi.org/10.1007/s00024-018-1976-9

Ito, Y., Obara, K., Shiomi, K., Sekine, S., & Hirose, H. (2007). Slow earthquake coincident with episodic tremors and slow slip events. *Science*, **315**, 503-506. https://doi.org/10.1126/science.1134454

Ji, Y., Yoshioka, S., & Matsumoto, T. (2016). Three-dimensional numerical modeling of temperature and mantle flow fields associated with subduction of the Philippine Sea plate, southwest Japan. *Journal of Geophysical Research: Solid Earth*, **121**, 4458-4482. https://doi.org/10.1002/2016JB0112912

Kano, M., Kato, A., Ando, R., & Obara, K. (2018). Strength of tremor patches along deep transition zone of a megathrust. *Scientific Reports*, **8**, 3655. https://doi.org/10.1038/s41598-018-22048-8

Kano, M., Kato, A., & Obara, K. (2019). Episodic tremor and slip silently invades strongly locked megathrust in the Nankai trough. *Scientific Reports*, **9**, 9270. https://doi.org/10.1038/s41598-019-45781-0

Kao, H., Wang, K., Dragert, H., Kao, J. Y., & Rogers, G. (2010). Estimating seismic moment magnitude (Mw) of tremor bursts in northern Cascadia: Implications for the "seismic efficiency" of episodic tremor and slip, *Geophysical Research Letters*, **37**, L19306. doi:10.1029/2010GL044927

Katsumata, A., & Kamaya, N. (2003). Low-frequency continuous tremor around the Moho discontinuity away from volcanoes in the southwest Japan, *Geophysical Research Letters*, **30**(1), 1020. https://doi.org/10.1029/2002GL015981

Kono, Y., Nakamoto, K., & Hiramatsu, Y. (2020). Temporal variation in seismic moment release rate of slow slips inferred from deep low-frequency tremors in the Nankai subduction zone. *Earth Planets Space*, **72,** 12. https://doi.org/10.1186/s40623-020-1142-3

Maeda, T., & Obara, K. (2009). Spatiotemporal distribution of seismic energy radiation from low-frequency tremor in western Shikoku, Japan. *Journal of Geophysical Research: Solid Earth*, **114**, B00A09. https://doi.org/10.1029/2008JB006043

Matsuzawa, T., Obara, K., & Maeda, T. (2009). Source duration of deep very low frequency earthquakes in western Shikoku, Japan, *Journal of Geophysical Research: Solid Earth*, **114**, B00A11, doi:10.1029/2008JB006044

Matsuzawa, T., Hirose, H., Shibazaki, B., & Obara, K. (2010) Modeling short- and long-term slow slip events in the seismic cycles of large subduction earthquakes. *Journal of Geophysical Research: Solid Earth*, **115**, B12301. https://doi.org/10.1029/2010JB007566

Maury, J., Ide, S., Cruz-Atienza, V. M., Kostoglodov, V., Gonzáles-Molina, G., & Péres-Campos, X. (2016). Comparative study of tectonic tremor locations: Characterization of slow earthquakes in Guerrero, Mexico. *Journal of Geophysical Research: Solid Earth*, **121**, 5136–5151. https://doi.org/10.1002/2016JB013027

Michel, S., Gualandi, A., & Avouac, J. P. (2019). Similar scaling laws for earthquakes and Cascadia slow-slip events. *Nature,* **574,** 522–526. https://doi.org/10.1038/s41586-019-1673-6

Mizukami, T., Yokoyama, H., Hiramatsu, Y., Arai, S., Kawahara, H., Nagaya, T., & Wallis, S. R. (2014). Two types of antigorite serpentinite controlling heterogeneous slow-slip behaviors of slab-mantle interface. *Earth and Planetary Science Letters*, **401**, 148-158. https://dx.doi.org/10.1016/j.epsl.2014.06.009

Nakano, M., Yabe, S., Sugioka, H., Shinohara, M., & Ide, S. (2019). Event size distribution of shallow tectonic tremor in the Nankai trough. *Geophysical Research Letters*, **46**, 5828–5836. https://doi.org/10.1029/ 2019GL083029

Nakata, R., Ando, R., Hori, T. & Ide, S. (2011). Generation mechanism of slow earthquakes: Numerical analysis based on a dynamic model with brittle–ductile mixed fault heterogeneity, *Journal of Geophysical Research: Solid Earth*, **116**, B08308, doi:10.1029/2010JB008188

Nakata, R., Hino, H., Kuwatani, T., Yoshioka, S., Okada, M., & Hori, T. (2017). Discontinuous boundaries of slow slip events beneath the Bungo Channel, southwest Japan. *Scientific Reports,* **7**, 6129. https://doi.org/10.1038/s41598-017-06185-0

Nakajima, J., & Hasegawa, A. (2016). Tremor activity inhibited by well-drained conditions above a megathrust. *Nature Communications*, **7**(1), 13863. https://doi.org/10.1038/ncomms13863

Neubert, K., & Brunner, E. (2007). A studentized permutation test for the non-parametric Behrens-Fisher problem. *Computational Statistics & Data Analysis*, **51**(10), 5192–5204. https://doi.org/10.1016/j.csda.2006.05.024

Nishikawa, T., Matsuzawa, T., Ohta, K., Uchida, N., Nishimura, T., & Ide, S. (2019). The slow earthquake spectrum in the Japan trench illuminated by the S-net seafloor observatories. *Science*, **365**, 808-813. https://doi.org/10.1126/science.aax5618

Obara, K. (2002). Nonvolcanic deep tremor associated with subduction in southwest Japan. *Science*, **296**, 1679-1681. https://doi.org/10.1126/science.1070378

Obara, K. (2010). Phenomenology of deep slow earthquake family in southwest Japan: Spatiotemporal characteristics and segmentation. *Journal of Geophysical Research: Solid Earth*, **115**, B00A25. https://doi.org/10.1029/2008JB006048

Obara, K., & Kato, A. (2016). Connecting slow earthquakes to huge earthquakes. *Science*, **353**(6296), 253-257. https://doi.org/10.1126/science.aaf1512

Obara, K., Tanaka, S., Maeda, T., & Matsuzawa, T. (2010). Depth-dependent activity of non-volcanic tremor in southwest Japan. *Geophysical Research Letters,* **37**, L13306. https://doi.org/10.1029/2010GL043679

Ozawa, S. (2017). Long-term slow slip events along the Nankai trough subduction zone after the 2011 Tohoku earthquake in Japan. *Earth Planets Space,* **69,** 56. https://doi.org/10.1186/s40623-017-0640-4

Ozawa S., Murakami, N., Kaidzu, M., Tada, T., Sagiya, T., Hatanaka, Y., Yarai, H., & Nishimura, T. (2002). Detection and monitoring of ongoing aseismic slip in the Tokai region, central Japan. *Science*, **298**, 1009–1012. https://doi.org/10.1126/science.1076780

Ozawa, S., Yarai, H., & Imakiire, T. (2013). Spatial and temporal evolution of the long-term slow slip in the Bungo Channel, Japan. *Earth Planet Space,* **65,** 67–73. https://doi.org/10.5047/eps.2012.06.009

Radiguet, M., Cotton, F., Vergnolle, M., Campillo, M., Walpersdorf, A., Cotte, N., & Kostoglodov, V. (2012). Slow slip events and strain accumulation in the Guerrero gap, Mexico. *Journal of Geophysical Research: Solid Earth*, **117**, B04305. https://doi.org/10.1029/2011JB008801

Rogers, G., & Dragert, H. (2003). Episodic tremor and slip on the Cascadia subduction zone: The chatter of silent slip. *Science*, **300**(5627), 1942–1943. https://doi.org/10.1126/science.1084783

Rousset, B., Campillo, M., Lasserre, C., Frank, W. B., Cotte, N., Walpersdorf, A., Socquet, A., & Kostoglodov, V. (2017). A geodetic matched-filter search for slow slip with application to the Mexico subduction zone. J*ournal of Geophysical Research: Solid Earth*, **122**, 10,498–10,514. https://doi.org/10.1002/2017JB014448

Schmidt, D. A., & Gao, H. (2010). Source parameters and time-dependent slip distributions of slow slip events on the Cascadia subduction zone from 1998 to 2008. *Journal of Geophysical Research: Solid Earth*, **115**, B00A18. https://doi.org/10.1029/2008JB006045

Sekine, S., Hirose, H., & Obara, K. (2010). Along-strike variations in short-term slow slip events in the southwest Japan subduction zone. *Journal of Geophysical Research: Solid Earth*, **115**, B00A27. https://doi.org/10.1029/2008JB006059

Shiomi, K., Matsubara, M., Ito, Y., & Obara, K. (2008). Simple relationship between seismic activity along Philippine Sea slab and geometry of oceanic Moho beneath southwest Japan. *Geophysical Journal International*, **173**, 1018–1029. https://doi.org/10.1111/j.1365-246X.2008.03786.x

Suito, H., & Ozawa, T. (2009). Transient crustal deformation in the Tokai district. *Journal of the Seismological Society of Japan*, **2**(61), 113–135. (in Japanese with English abstract)

Supino, M., Poiata, N., Festa, G., Vilotte, J. P., Satriano, C., & Obara, K. (2020). Self-similarity of low-frequency earthquakes. *Scientific Reports,* **10,** 6523. https://doi.org/10.1038/s41598-020-63584-6

Sweet, J. R., Creager, K. C., Houston, H., & Chestler, S. R. (2019). Variations in Cascadia low-frequency earthquake behavior with downdip distance. *Geochemistry, Geophysics, Geosystems*, **20**, 1202−1217. https://doi.org/10.1029/2018GC007998

Takagi, R., Obara, K., & Maeda, T. (2016). Slow slip event within a gap between tremor and locked zones in the Nankai subduction zone. *Geophysical Research Letters,* **43**, 1066–1074. https://doi.org/10.1002/2015GL066987

Tanaka, Y., Suzuki, T., Imanishi, Y. (2018). Temporal gravity anomalies observed in the Tokai area and a possible relationship with slow slips. *Earth Planets Space*, **70,** 25. https://doi.org/10.1186/s40623-018-0797-5

Ueno, T., Maeda, T., Obara, K., Asano., Y., & Takeda, T. (2010) Migration of low-frequency tremors revealed from multiple–array analyses in western Shikoku, Japan. *Journal of Geophysical Research: Solid Earth,* **115**, B00A26. https://doi.org/10.1029/2008JB006051

Wallace, L. M., & Beavan, J. (2010). Diverse slow slip behavior at the Hikurangi subduction margin, New Zealand. *Journal of Geophysical Research: Solid Earth*, **115**, B12402. https://doi.org/10.1029/2010JB007717

Watanabe, T., Hiramatsu, Y., & Obara, K. (2007). Scaling relationship between the duration and the amplitude of non-volcanic deep low-frequency tremors. *Geophysical Research Letters,* **34**, L07305. https://doi.org/10.1029/2007GL029391

Wessel, P., & Smith, W. H. G. (1998). New improved version of the generic mapping tools released. *Eos Trans. AGU*, **79**, 579

Yabe, S., & Ide, S. (2014). Spatial distribution of seismic energy rate of tectonic tremors in subduction zones. *Journal of Geophysical Research: Solid Earth*, **119**, 8171–8185. https://doi.org/10.1002/2014JB011383

Figure captions

Figure 1. (a) Distribution of tectonic tremor events (dots) and the location of the study area around the Bungo Channel (rectangle, indicating the area of the map in the left panel of (b)). Green dashed lines indicate depth contours of the subducting Philippine Sea plate (Shiomi et al., 2008). (b) Spatial (left panel) and temporal (right panel) distributions of tremor epicenters (dots, from the NIED hybrid clustering catalogue; Obara et al., 2010) and Hi-net stations (blue triangles) used in this study. Red dots represent tremor events at grid points with tentative excitation ratios exceeding 4.0 (see section 3.3). The magenta circle shows the location of the event for which the reduced displacement waveform is shown in Figure 2a. In the right panel of (b), blue and red bars indicate

periods during which L-SSEs were geodetically observed (Ozawa, 2017; Ozawa et al., 2013) and tremor-excitation periods (see section 3.3 for the definition of the tremor-excitation periods), respectively, and gray-shaded areas represent periods in which an L-SSE occurred in central-western Shikoku (Takagi et al., 2016; excluded from this study). The color scale in the right panel of (b) denotes the value of the characteristic amplitude (CA) of each tremor event analyzed in this study, whereas black circles indicate tremor events that were not analyzed.

Figure 2. (a) Example of the reduced displacement (D_R) of a tremor event recorded at station KWBH at 19:00 JST on 19 September 2006. The location of the event is shown by the magenta circle in the left panel of Figure 1b. Vertical dashed black lines mark the start and end times of the tremor event. The horizontal dashed red line indicates the noise level at that station around the time of the tremor event. The blue line is the threshold value (D_R^*), and parts of the waveform used to measure tremor duration (i.e., exceeding the threshold value) are traced in green (see section 3.2). (b) Exponential and (c) power-law models of the waveform shown in (a). The red lines in (b, c) are the best fit to the models.

Figure 3. Frequency distributions of the coefficient of determination, R^2, for the (a) exponential and (b) power-law models.

Figure 4. (a) The cumulative apparent moment for all events in the study area and period. (b) The smoothed cumulative apparent moment for only those events at grid points with tentative excitation ratios exceeding 4.0 (see section 3.3). (c) Temporal variations of the apparent moment rate calculated from (b); solid, dotted, and dashed horizontal lines indicate one, two, and five times the average apparent moment rate during inter-LSSE periods. Red circles indicate events that meet criteria (1)–(3) for determining tremor-excitation periods (see section 3.2), whereas events indicated by blue circles only meet one or two criteria. Blue and red bars and gray-shaded areas are as in Figure 1b.

Figure 5. Correlations of CA with (a) apparent moment and (b) apparent moment rate. *R* and *p* denote the correlation coefficient and *p*–value, respectively. Gray dashed lines in (a) highlight the relation between CA and apparent moment (= CA$\cdot$ d_t) for specific values of d_t. The color scale indicates observed tremor duration.

Figure 6. Cumulative frequency plots of CA during tremor-excitation periods (upper panels) and inter-L-SSE periods (lower panels) at the grid point outlined by the black square in Figure 7a and 7b. Left and right panels show exponential and power-law fits to the distribution, respectively. Red

lines show the best-fit line and R^2 indicate the coefficient of determination for each distribution for CA $\geq$ 5×10^{-6} m^2.

Figure 7. Spatial distributions of (a) the median CA value during tremor-excitation periods, (b) the median CA value during inter-L-SSE periods, (c) ΔCA_1 (= $CA_{\text{tremor–excitation}} - CA_{\text{inter-L-SSE}}$), and (d) the statistical significance (*p*-values) of ΔCA_1. Green dashed lines show areas in which the slip was greater than 0.2 m and 0.1 m during the 2010 L-SSE (Nakata et al., 2017). Zones A, B, and C (bounded by black rectangles) denote areas in which ΔCA_1 is positive, negative, or near zero, respectively.

Figure 8. Spatial distributions of the median CA value and ΔCA_2 (= $CA_{\text{L-SSE + tremor-excitation}} - CA_{\text{inter-L-SSE}}$) for the L-SSEs in (top panels) 2003, (middle panels) 2010, and (bottom panels) 2014. All symbols are as in Figure 7.

Figure 9. Spatial distributions of the median CA value during L-SSEs prior to tremor-excitation periods and ΔCA_3 (= $CA_{\text{L-SSE – tremor-excitation}} - CA_{\text{L-SSE + tremor–excitation}}$) for the L-SSEs in (top panels) 2003 and (middle panels) 2010, and (bottom panels) the stacked data for both L-SSEs. All symbols are as in Figure 7.

Figure 10. Changes of the CA distributions between tremor-excitation periods (L-SSE periods) and inter-L-SSE periods. (a) The spatial distribution of grid points at which ΔCA_1 is greater than 1.0 (red, zone A) and lower than –1.0 (blue, zone B). ΔCA_1 values between –1.0 and 1.0 are omitted from this plot to reduce fluctuations in CA. Frequency distributions of tremor CA values are shown for (b) zone A and (c) zone B during (upper) tremor-excitation periods, (middle) inter-L-SSE periods, and (lower) the change of the distributions between the two periods.

Figure 11. Schematic diagram of the plate interface beneath the Bungo Channel (zone A). (upper) During inter-L-SSE periods, high pore-fluid pressure (light blue area) caused by dehydration (light blue arrows) of the subducting slab generates tectonic tremor in the ETS zone (pink zone). (lower) During tremor-excitation periods, L-SSEs (red zone) induce increased stress in the ETS zone and result in upward fluid migration (open purple arrow), causing high-CA tremors in the up-dip part of the ETS zone (the area enclosed by the dashed line).

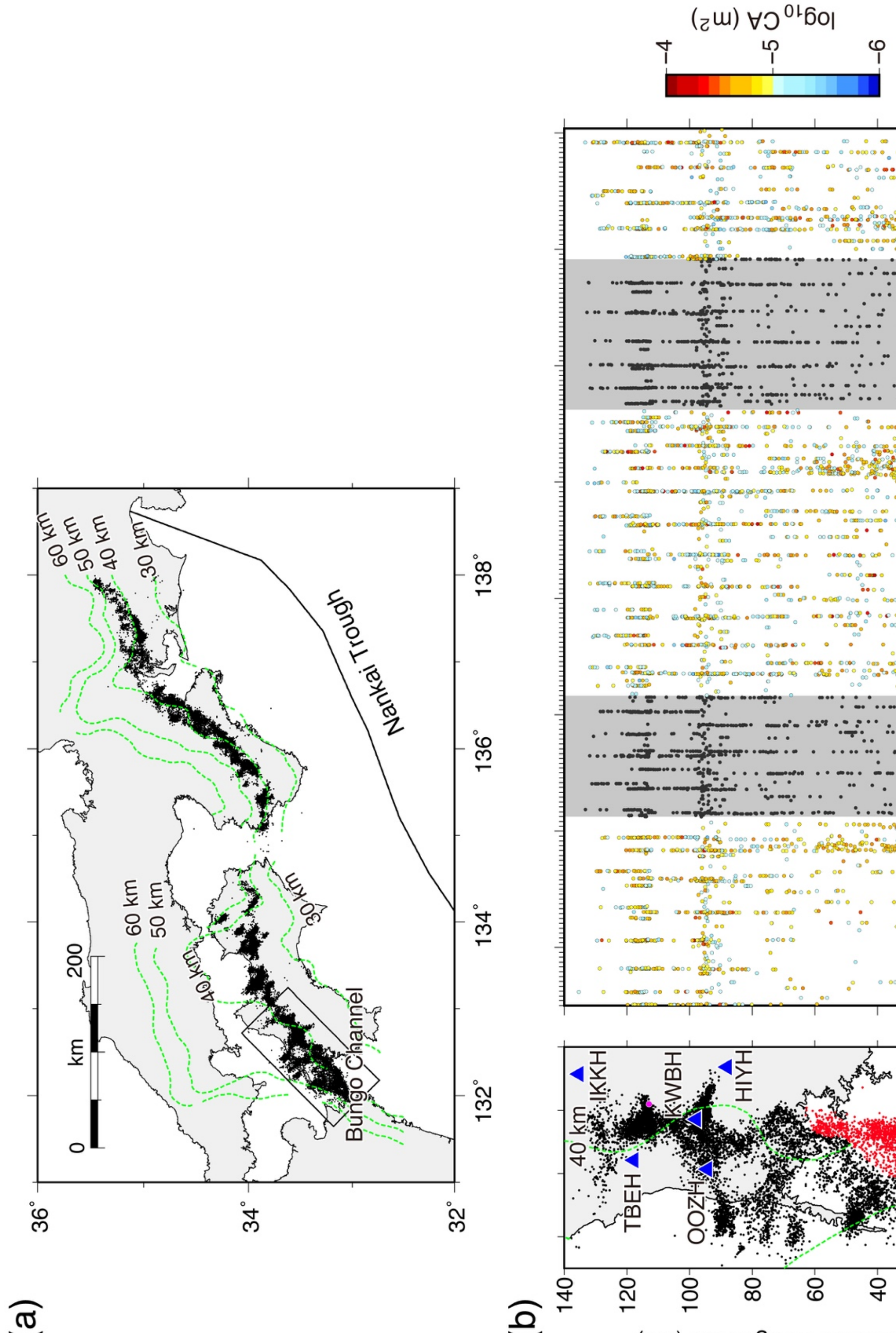
(a)
(b)
Nankai Trough
Bungo Channel
km
60 km
50 km
40 km
30 km
TBEH
IKKH
KWBH
OOZH
HIYH
Distance along strike (km)
Distance along dip (km)
Time (year)
log10 CA (m2)

Figure 1.

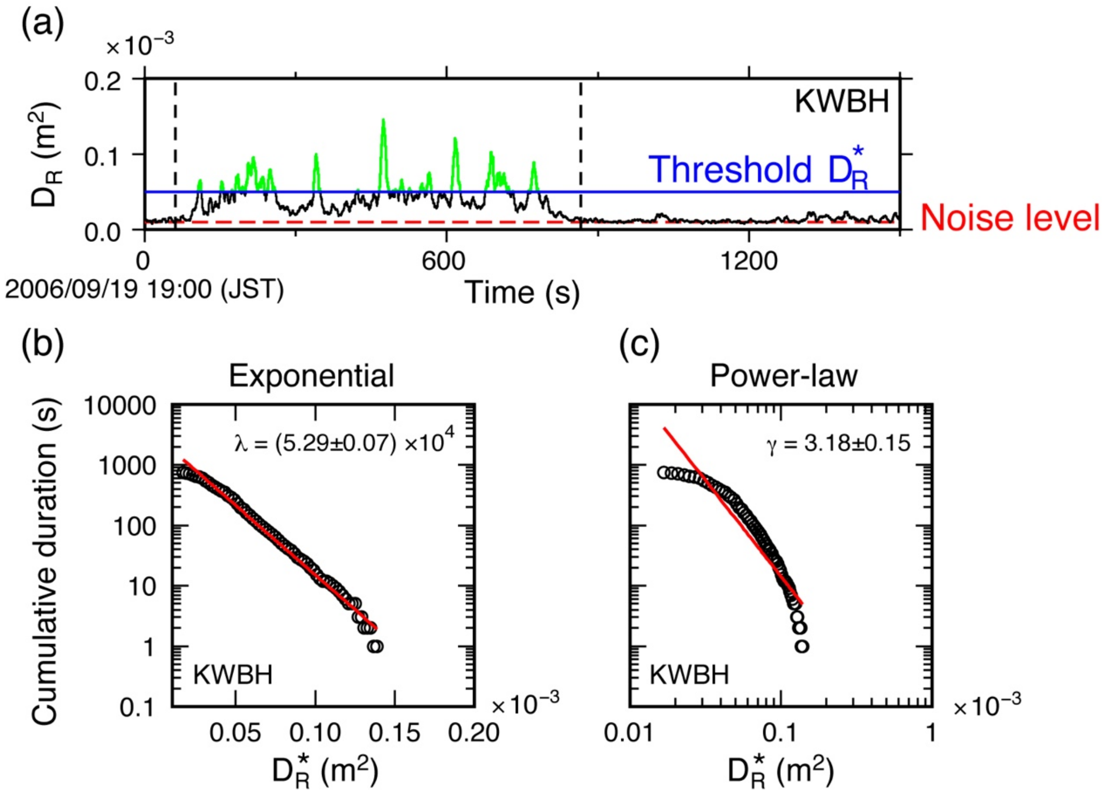
(a)
×10⁻³
KWBH
Threshold D_R^*
Noise level
D_R (m²)
2006/09/19 19:00 (JST)
Time (s)
(b)
Exponential
λ = (5.29±0.07) ×10⁴
KWBH
Cumulative duration (s)
D_R^* (m²)
(c)
Power-law
γ = 3.18±0.15
KWBH
D_R^* (m²)

Figure 2.

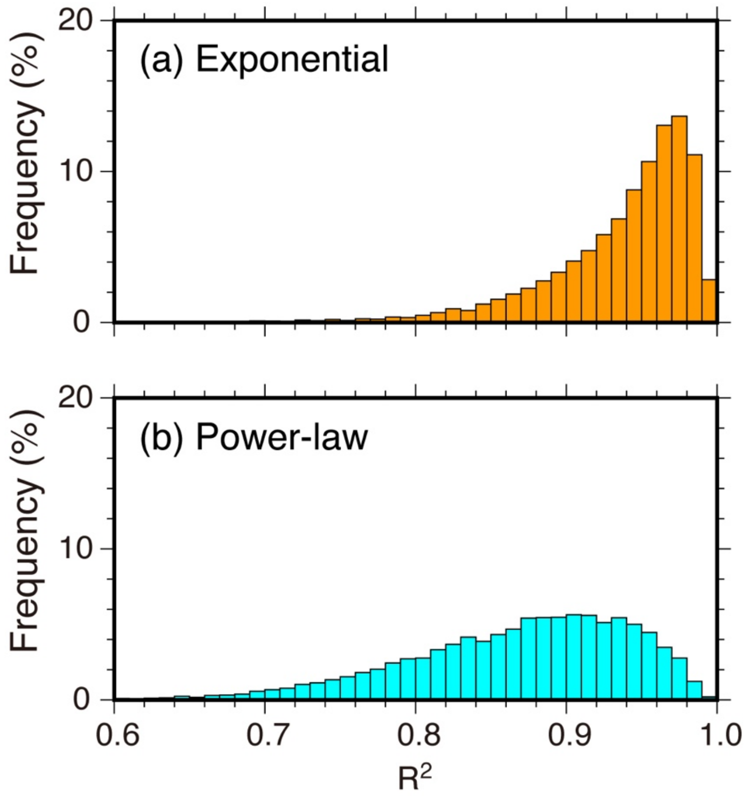

(a) Exponential
Frequency (%)
0
10
20
(b) Power-law
Frequency (%)
0
10
20
0.6
0.7
0.8
0.9
1.0
R^2

Figure 3.

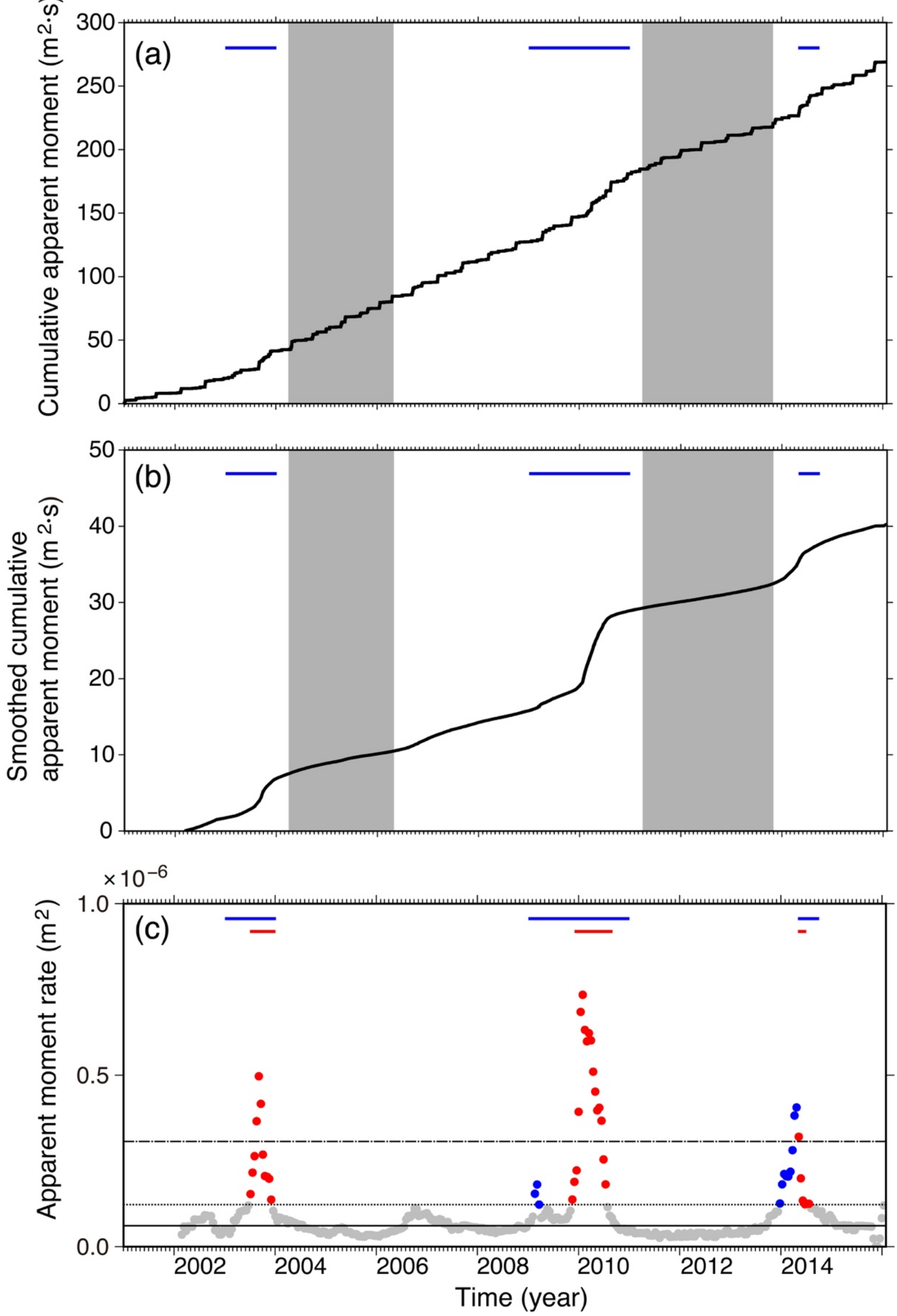

(a)
Cumulative apparent moment (m^2·s)
300
250
200
150
100
50
0
(b)
Smoothed cumulative apparent moment (m^2·s)
50
40
30
20
10
0
(c)
×10^{-6}
Apparent moment rate (m^2)
1.0
0.5
0.0
2002
2004
2006
2008
2010
2012
2014
Time (year)

Figure 4.

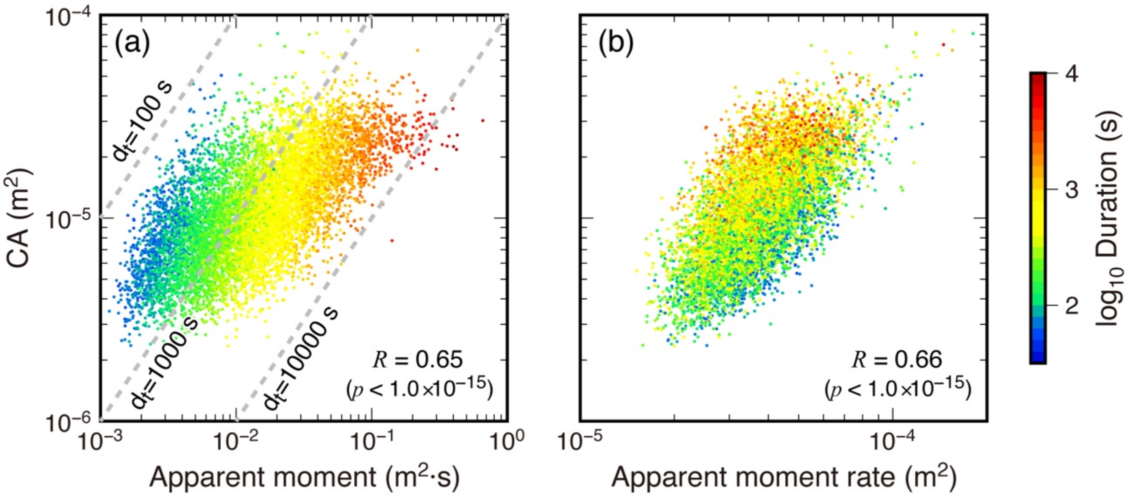

(a)
(b)
CA (m^2)
10^{-4}
10^{-5}
10^{-6}
d_t=100 s
d_t=1000 s
d_t=10000 s
R = 0.65
(p < 1.0×10^{-15})
10^{-3}
10^{-2}
10^{-1}
10^{0}
Apparent moment (m^2·s)
R = 0.66
(p < 1.0×10^{-15})
10^{-5}
10^{-4}
Apparent moment rate (m^2)
$\log_{10}$ Duration (s)
4
3
2

Figure 5.

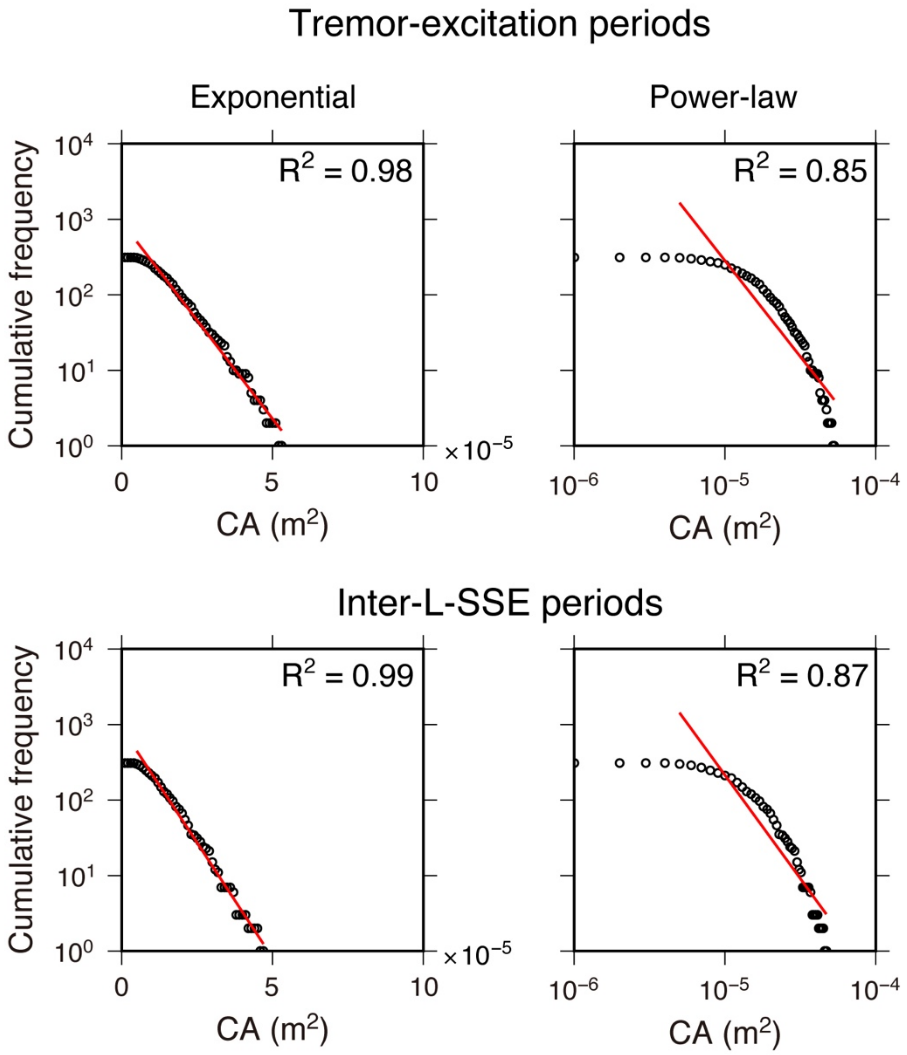

Tremor-excitation periods
Exponential
Power-law
Cumulative frequency
$R^2 = 0.98$
$R^2 = 0.85$
10^4
10^3
10^2
10^1
10^0
0
5
10
$\times 10^{-5}$
10^{-6}
10^{-5}
10^{-4}
CA (m^2)
Inter-L-SSE periods
$R^2 = 0.99$
$R^2 = 0.87$

Figure 6.

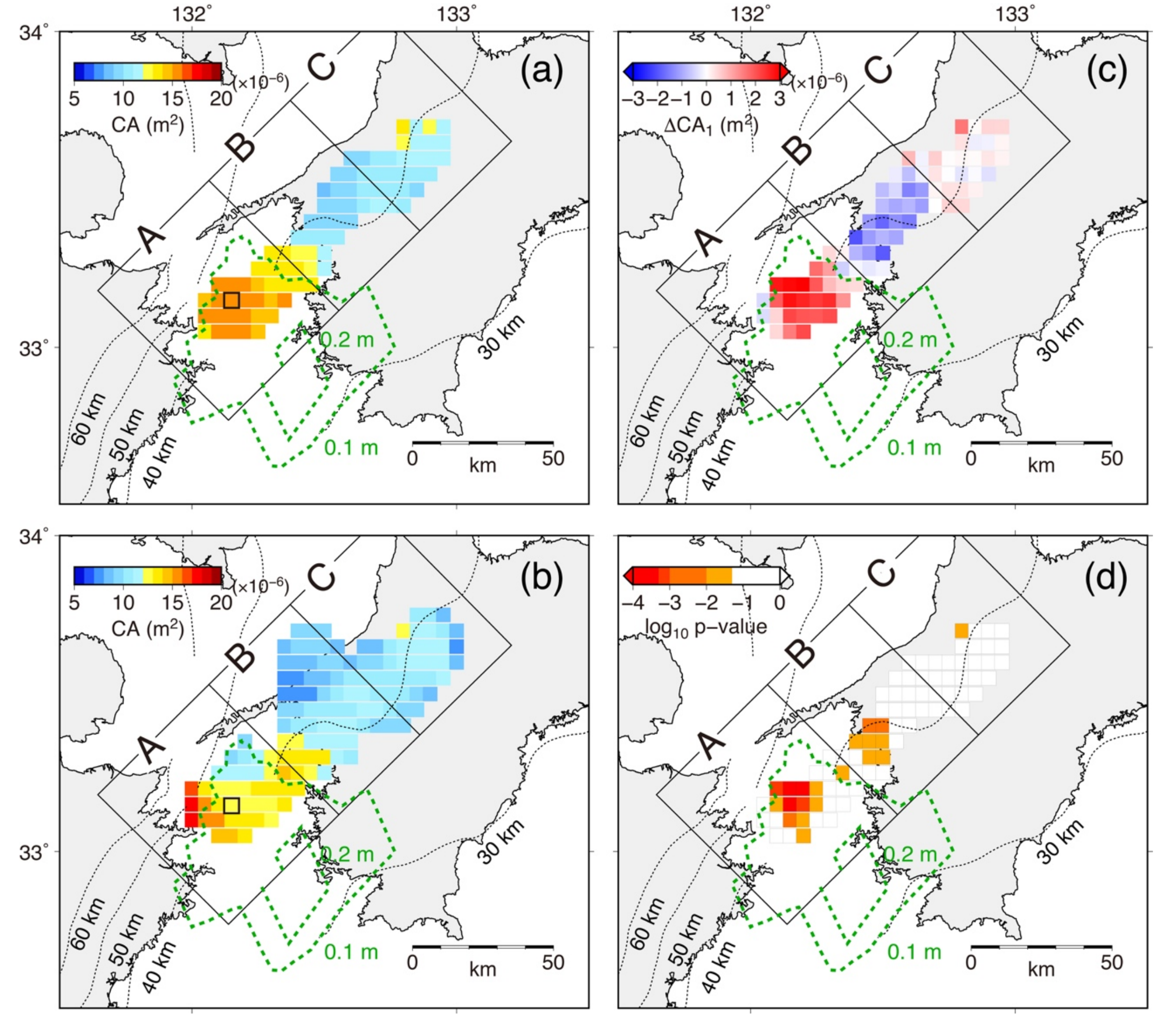

(a)
(b)
(c)
(d)
A
B
C
132°
133°
34°
33°
CA (m^2)
5 10 15 20
(×10^{-6})
ΔCA$_1$ (m^2)
−3 −2 −1 0 1 2 3
log$_{10}$ p-value
−4 −3 −2 −1 0
0.2 m
0.1 m
30 km
40 km
50 km
60 km
0 km 50

Figure 7.

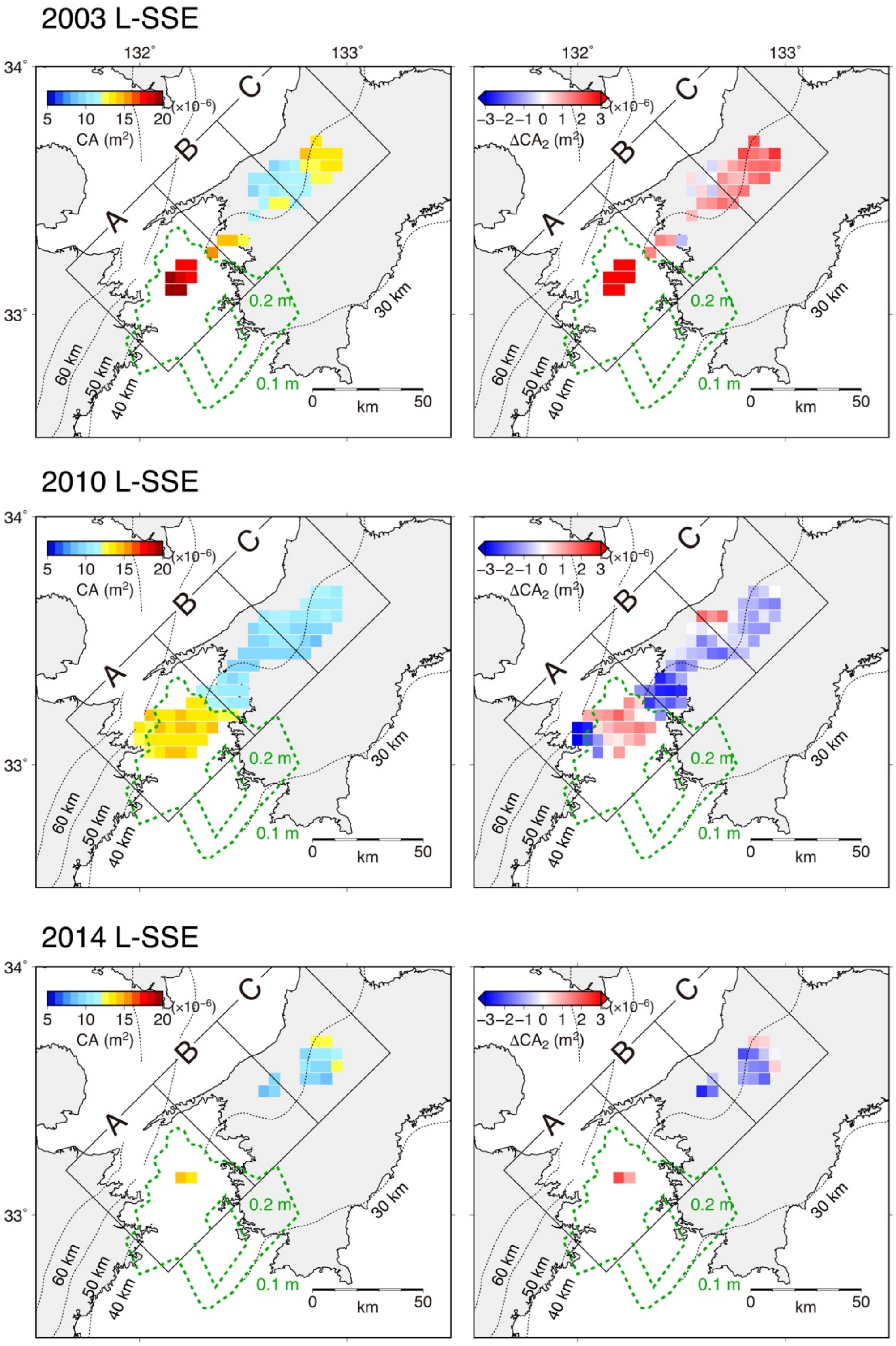
2003 L-SSE
2010 L-SSE
2014 L-SSE
132°
133°
34°
33°
CA (m2)
(×10−6)
5 10 15 20
ΔCA2 (m2)
−3 −2 −1 0 1 2 3
A
B
C
0.2 m
0.1 m
30 km
40 km
50 km
60 km
0 km 50

Figure 8.

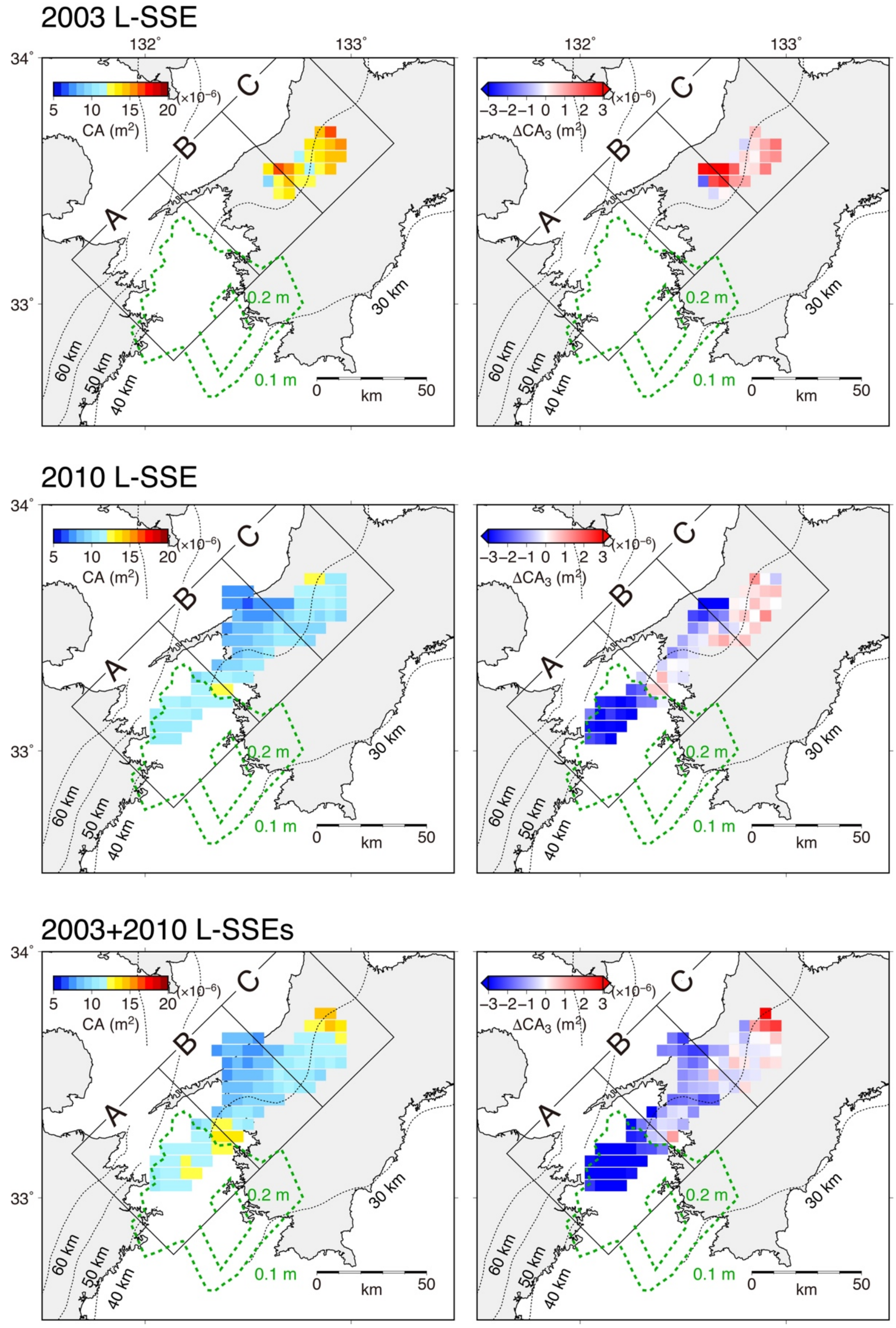

2003 L-SSE
2010 L-SSE
2003+2010 L-SSEs
132°
133°
34°
33°
CA (m2)
(×10−6)
5
10
15
20
ΔCA3 (m2)
−3
−2
−1
0
1
2
3
A
B
C
0.2 m
0.1 m
30 km
40 km
50 km
60 km
km
0
50

Figure 9.

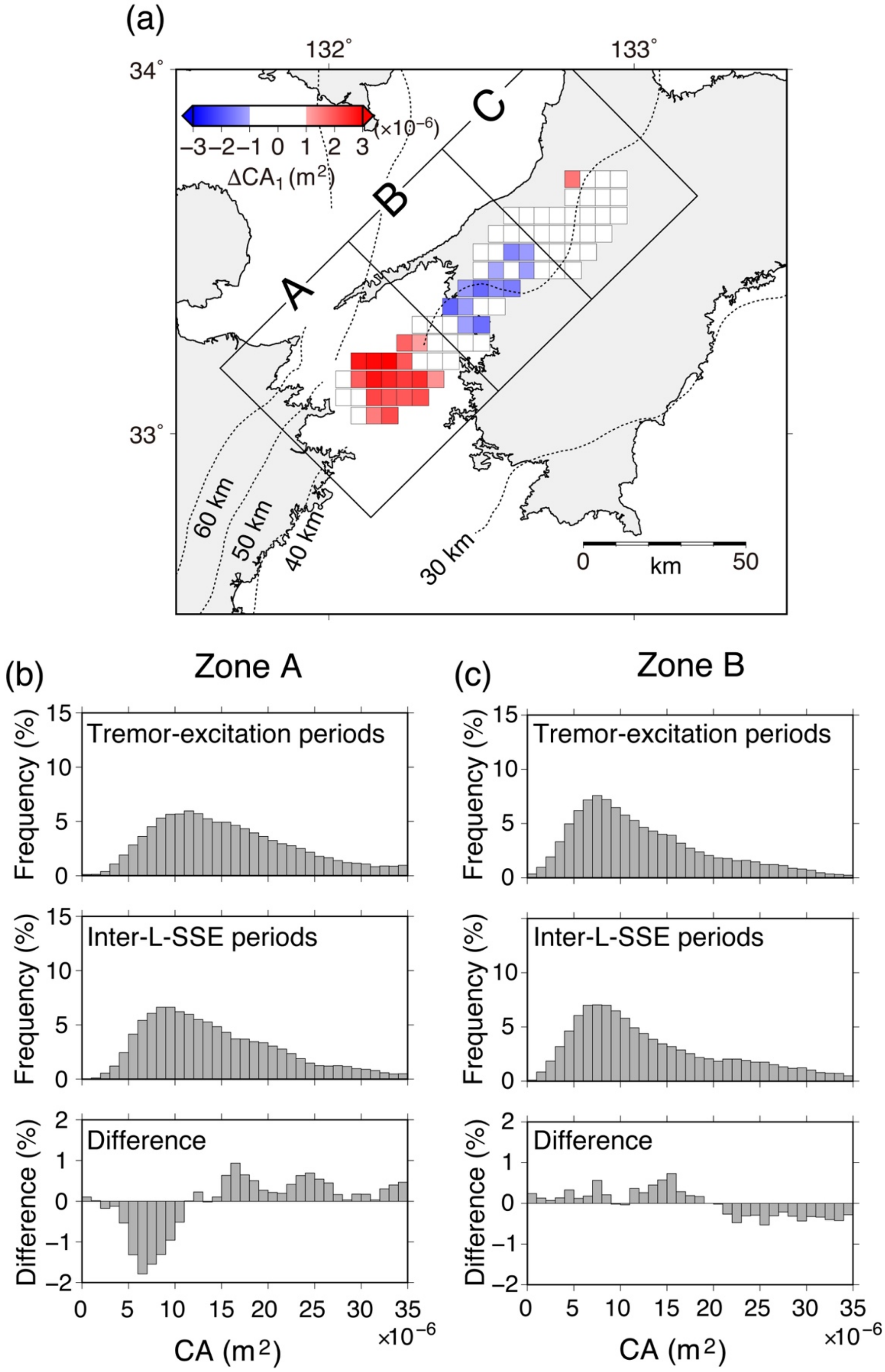

(a)
132°
133°
34°
33°
A
B
C
−3 −2 −1 0 1 2 3
(×10−6)
ΔCA1 (m2)
60 km
50 km
40 km
30 km
0
km
50
(b)
Zone A
(c)
Zone B
Tremor-excitation periods
Inter-L-SSE periods
Difference
Frequency (%)
Difference (%)
CA (m2)
×10−6

Figure 10.

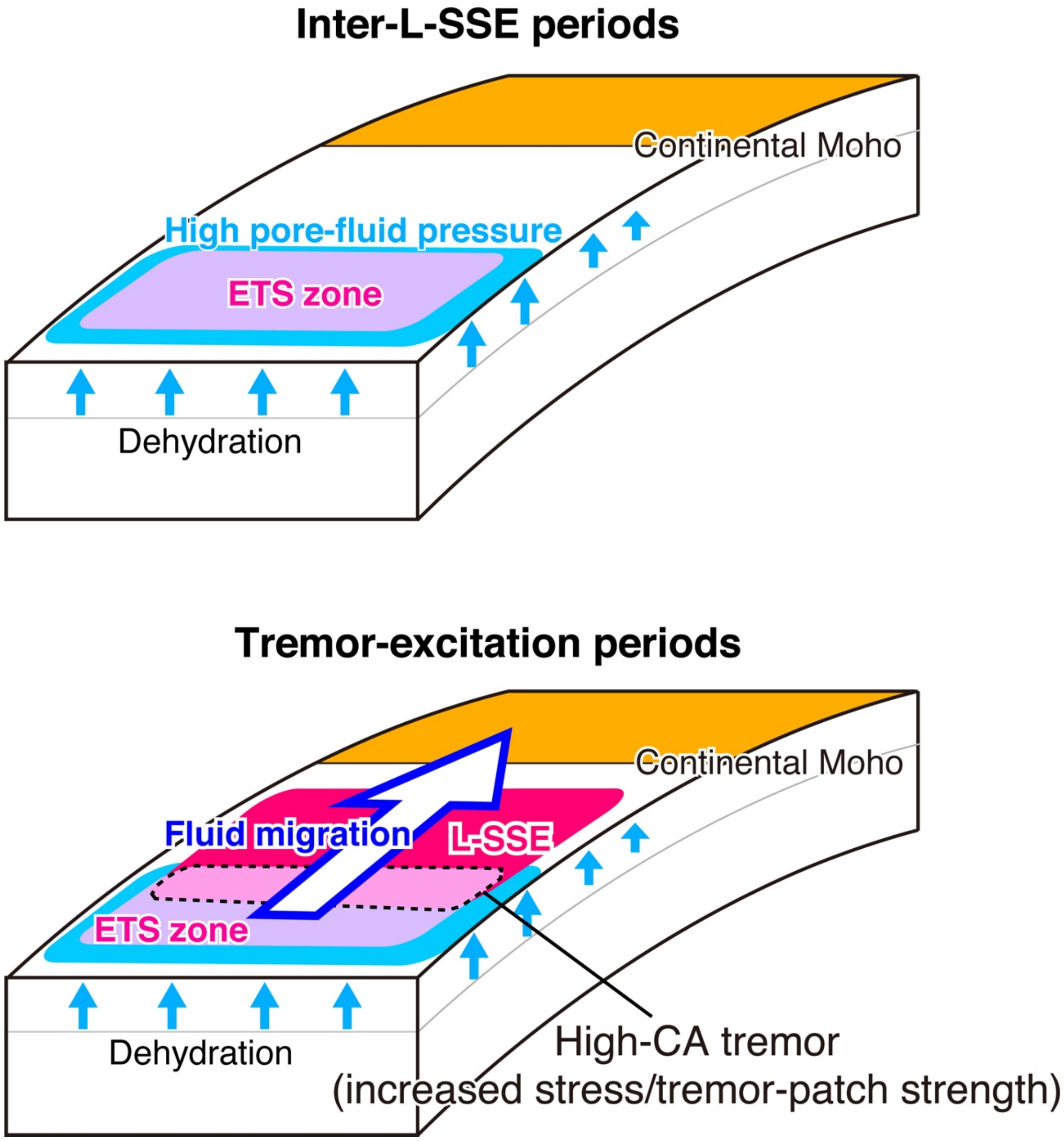

Inter-L-SSE periods
Continental Moho
High pore-fluid pressure
ETS zone
Dehydration
Tremor-excitation periods
Continental Moho
Fluid migration
L-SSE
ETS zone
Dehydration
High-CA tremor
(increased stress/tremor-patch strength)

Figure 11.